**RESEARCH OUTLINE:**

**I. Shape-Preserving Chemical Transformation: "Materials Alchemy"**

***A. Shape-Preserving Liquid/Solid Displacement Reactions***

Example: High-Melting, Robust ZrC/W Rocket Nozzles via the "Displacive Compensation of Porosity" Process

***B. Shape-Preserving Gas/Solid Displacement Reactions***

Example: Highly-Porous Si Films on Dense, Si Waveguides as IR Sensors via a Magnesiothermic Reduction Process

***C. Conformal Coating and Replication***

Example: Porous Wall, Nanocrystalline $TiO_2$ Nanotube Arrays for Solar Cells and Other Electrode Applications

**II. Bio-enabled, Chemically-Tailored, Hierarchically-Structured Materials**

***A. Diatom-Enabled 3-D Materials***

Examples: 1. Si, C, $TiO_2$, and Other Replicas via Gas/Solid Reactions for Battery and Fuel Cell Electrodes, Enzyme Supports, Sensors
2. Au Replicas via Conformal Electroless Deposition for Extraordinary Optical Transmission

***B. Butterfly-Enabled 3-D Materials***

Example: Photoluminescent Eu-doped $BaTiO_3$ Replicas via Layer-by-Layer Surface Sol-Gel Coating and Hydrothermal Reaction for Anti-Counterfeiting and Tracking

***C. Pollen-Enabled 3-D Materials***

Example: Magnetic $Fe_3O_4$ Replicas via Layer-by-Layer Surface Sol-Gel Coating for Tailored Multimodal Adhesion

***D. Protein-Enabled Hybrid Coatings***

Example: Enzyme/Oxide Coatings via Layer-by-Layer Protamine-based Deposition for Biocatalysis

**RESEARCH DESCRIPTIONS:**

**I. Shape-Preserving Chemical Transformation: "Materials Alchemy"**

Materials with complex three-dimensional (3-D) morphologies, and with tailorable micro-to-nanoscale structures and chemistries, are needed to achieve desired combinations of properties for enhanced performance in a host of energy, environmental, transportation, defense, and medical applications. However, materials that can be easily formed into a particular desired morphology often do not possess the required chemistry and finer scale structure needed for desired properties. This problem may be addressed by separating the shape-forming process from the chemical-tailoring process; that is, a solid structure with the desired shape (a "preform") may first be generated with a readily-formed material and then a second, shape-preserving reaction process may be used to convert this preform into a new material with a desired chemistry and

micro/nanostructure. Several pioneering shape-preserving chemical transformation processes (see below) have been developed and patented by the Sandhage group to convert synthetic preforms (e.g., generated by 3-D printing or CNC machining) and biogenic preforms (e.g., diatom microshells, butterfly scales, pollen grains) into complex-shaped, chemically-tailored, micro/nanostructured materials with attractive properties. Such shape-preserving chemical transformation of one material into another may be considered to be a modern type of materials "alchemy." Several examples are presented below of the use of such processes to generate macroscale/microstructured and microscale/nanostructured materials with well-controlled chemistries and morphologies for particular applications.

### *A. Shape-Preserving Liquid/Solid Displacement Reactions:* High-Melting, Robust ZrC/W Rocket Nozzles via the "Displacive Compensation of Porosity" Process

One of the most severe environments encountered by materials exists in the throat region of a solid-fueled rocket nozzle. Solid, aluminum-bearing fuels generate combustion products (molten $Al_2O_3$ droplets and gas) that impact the nozzles at supersonic speeds and at temperatures >2500$^o$C. Under these extreme conditions, rocket nozzle materials need to exhibit minimal vaporization, erosion, and creep. Nozzle materials must also be highly resistant to thermal shock, given the rapid rise in temperature upon ignition. Conventional materials used for such solid-fuel nozzles include tungsten, rhenium, and carbon. Tungsten and rhenium are quite heavy, and all three materials are not highly erosion resistant at elevated temperatures.

Zirconium carbide/tungsten (ZrC/W) composites are attractive alternative materials for solid-fuel rocket nozzles. Zirconium carbide is a stiff, hard, high-melting (up to 3445$^o$C) compound that is much lighter (6.6 g/cm$^3$) than tungsten (19.3 g/cm$^3$). Tungsten is also quite high-melting (3422$^o$C) but undergoes a brittle-to-ductile transformation at ≤360$^o$C. Hence, an interconnected ZrC network endows ZrC/W composites with high-temperature stiffness and reduced weight relative to monolithic W, whereas the high-temperature ductility of W provides higher resistance to fracture at elevated temperatures relative to monolithic ZrC. ZrC and W are also chemically and thermally compatible. ZrC and W possess low vapor pressures and exhibit limited mutual solid solubility at elevated temperature. Furthermore, these solids do not react to form other more stable compounds. Remarkably, ZrC and W possess similar thermal expansion coefficients at room temperature and at 2700$^o$C, and both materials possess relatively high values of thermal conductivity. As a result, ZrC/W composites are highly resistant to thermal shock (unlike most ceramic/metal composites).

A pressureless reactive melt infiltration process developed and patented by Sandhage, et al. has been used to fabricate ZrC/W (and other) cermets into complicated near net-shape/size bodies. With this "Displacive Compensation of Porosity" (DCP) process, porous WC bodies ("preforms") are first produced in the desired final 3-D shape via conventional forming (such as by pressing, slip casting, or gel casting) or via rapid prototyping methods (such as 3-D printing or CNC green machining). Once the porous

WC preform has been fabricated into the desired final shape, it is then immersed in a bath of $Zr_2Cu$ liquid at 1150°C which wets and spontaneously infiltrates into the porous WC preform. Upon heating to 1300°C, the following displacement reaction proceeds to completion:

$$0.5Zr_2Cu(l) + WC(s) \Rightarrow ZrC(s) + W(s) + 0.5Cu(l)$$

Because ZrC and W possess a combined volume about twice that of WC, the reaction results in filling of the prior pores within the rigid body (reaction-induced ***densification without sintering***), thereby forcing the residual Cu-rich liquid back out of the composite; that is, the increase in solid volume due to the displacement reaction compensates for the prior pore volume (hence, the phrase "Displacive Compensation of Porosity"). As shown in **Figures 1** and **2**, porous 3-D WC parts have been fully converted into non-porous ZrC/W-based composites that retain the starting preform 3-D shape with very small dimensional changes (fractional changes $\leq$0.008).

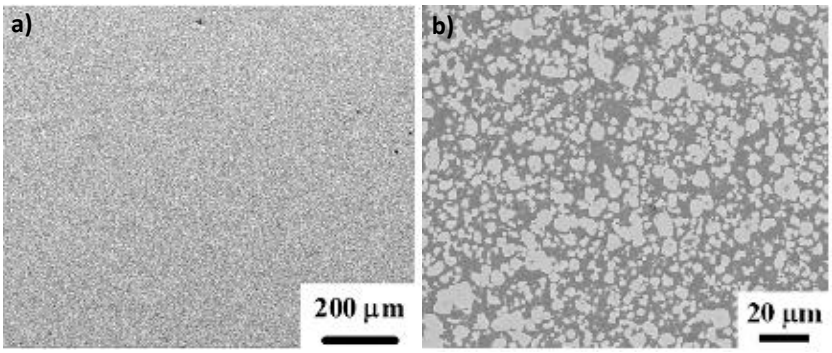


**Figure 1.** Cross-sectional images of a dense ZrC/W composite prepared by pressureless infiltration of $Zr_2Cu(l)$ into porous WC at 1150°C, then complete reactive conversion at 1300°C (DCP process): a) low magnification secondary electron image of the dense cermet, b) higher magnification backscattered electron image of the grey ZrC matrix and brighter W particles.


| d Specimen Description | Outer Dia. @ Exit | Outer Dia. @ Entrance | Nozzle Height |
|---|---|---|---|
| Porous 3-D printed WC preform | 54.23 ± 0.25 mm | 40.34 ± 0.20 mm | 34.82 ± 0.15 mm |
| ZrC/W nozzle (after reaction) | 53.90 ± 0.12 mm | 40.09 ± 0.13 mm | 34.53 ± 0.23 mm |
| | $\Delta D/D_o$ = -0.61% | $\Delta D/D_o$ = -0.62% | $\Delta L/L_o$ = -0.83% |

**Figure 2.** Demonstration of net-shape/size DCP processing (of rocket nozzles). a) Porous, rigid WC nozzle preform prepared by 3-D printing, then binder burnout and light sintering (to neck WC particles to enhance preform rigidity). b), c) ZrC/W nozzles formed by immersing the porous WC preform in $Zr_2Cu(l)$ at 1150°C, then reaction above the melt at 1300°C. Adherent Cu-rich metal on the surface of the specimen in b) (pushed out from inside the specimen during the pore-filling DCP reaction) was removed from the specimen in c). d) Measured dimensions are shown of a reactively-converted nozzle in c), and of the associated porous WC preform prior to infiltration (dimensional changes were $\leq$ 0.85%).

Because this reaction process is rate-limited by outward solid-state diffusion of C from local WC particles through the ZrC/W reaction products, the time required to complete this reaction does not depend on the size of the preform, so that the DCP process is scalable to much larger parts than shown in **Figure 2**.

The DCP process is a proven means of producing dense, near net-shape/size, ZrC/W composites (and other cermets) in a variety of complex and tailorable 3-D shapes (e.g., rocket nozzles, nozzle liners, grooved plates, crucibles, etc.). These and other DCP-

derived cermets possess an unusual combination of properties for extreme (e.g., highly erosive, high temperature, high thermal shock, corrosive) environments. Indeed, DCP-derived ZrC/W rocket nozzle liners (**Figure 3**) were found to be resistant to the extreme thermal shock and erosion of a solid-fueled Pi-K rocket test conducted at Edwards Air Force Base (in collaboration with Dr. Wes Hoffman).


**Figure 3.** ZrC/W rocket nozzle liners fabricated by: a) gel-casting to generate a porous WC nozzle liner, b) immersion of the porous WC nozzle liner in molten $Zr_2Cu$ at 1200°C for 10 min, and c) completion of the DCP reaction upon heating to 1300°C to yield dense, near net-shape and near net-size ZrC/W nozzle liners. Such liners placed within a carbon composite backing material yield lightweight nozzles resistant to the extreme thermal shock and erosion of a solid-fuel Pi-K rocket test.

### *B. Shape-Preserving Gas/Solid Displacement Reactions:* Highly-Porous Si Films on Dense, Micropatterned Si Waveguides as IR Sensors via a Magnesio-thermic Reduction Process

Owing to its attractive optical and electrical properties, large surface-to-volume ratio, and ease of surface modification, porous silicon (pSi) has been extensively studied in a variety of applications, such as light-emitting diodes, photodetectors, optical switches, lithium ion batteries, and label-free optical detection of numerous analytes (bacteria, enzymes, viruses, DNA, gases). Conventionally, pSi films are fabricated by anodization of single crystal silicon wafers, leading to films possessing two-dimensional (2-D), cylindrical mesopores with thicknesses controlled by the anodization kinetics of doped silicon in HF-bearing solutions. The use of applied currents with HF-bearing solutions makes integration with silicon-on-insulator (SOI) platforms difficult. Furthermore, such anodized pSi optical microcavities have exhibited modest quality factors.

The Sandhage group has developed and patented a magnesiothermic reaction process that yields pSi films with three-dimensionally-interconnected nanoporosity on SOI platforms that avoids the need for doped silicon, applied currents, or HF-bearing solutions. With this process, unpatterned SOI substrates are first oxidized to yield a $SiO_2$ thin film of well-controlled thickness. The silica film is then allowed to undergo the following magnesiothermic displacement reaction:

$$SiO_2(s) + 2Mg(g) \Rightarrow 2MgO(s) + Si(s)$$

The resulting product film is comprised of an intimate mixture of nanocrystalline MgO and Si phases that form as co-continuous networks. This reaction process has been thermodynamically designed to allow for reaction of the Mg(g) with only the $SiO_2$ film (i.e., not with the underlying Si substrate), so that the thickness of the pSi film can be

precisely controlled via adjustment of the starting $SiO_2$ film thickness (which is itself tailorable to within ~1 nm by controlled thermal oxidation of silicon). Selective acid dissolution of the continuous MgO phase then yields a 3-D-interconnected network of nanosized pores and an interconnected network of nanocrystalline Si (**Figure 4**).

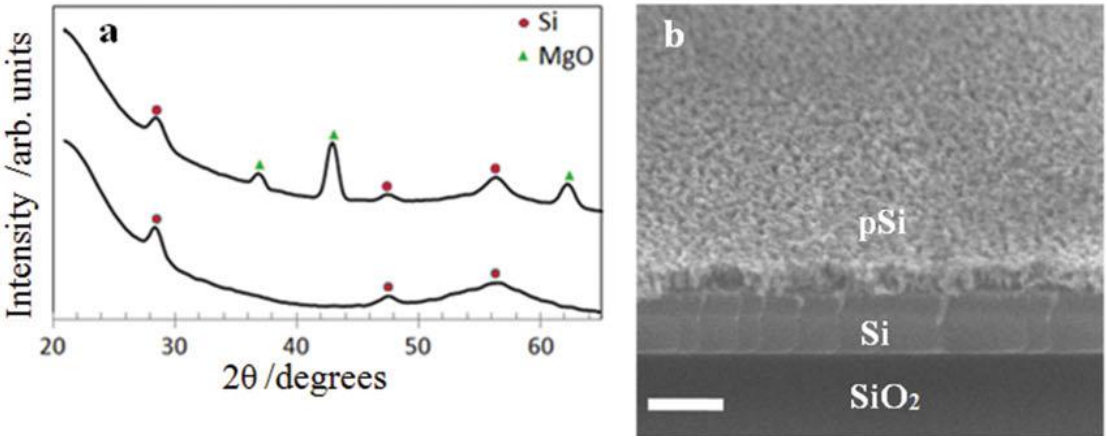


**Figure 4.** Characterization of pSi generated via shape-preserving magnesiothermic conversion. a) Grazing incidence X-ray diffraction analysis of converted blanket silica films on SOI: (top) MgO/Si film and (bottom) pSi film after selective MgO dissolution. b) Secondary electron image of a magnesiothermically-formed pSi layer on a SOI substrate (scale bar = 500 nm).

After selective MgO dissolution, the resulting pSi-clad Si specimens were patterned into pSi-clad optical resonators (**Figure 5**) in collaborative research with the Adibi group (School of Electrical and Computer Engineering) at Georgia Tech. The pSi-clad SOI racetrack microresonators consisted of a ~120 nm thick pSi cladding on a ~520 nm

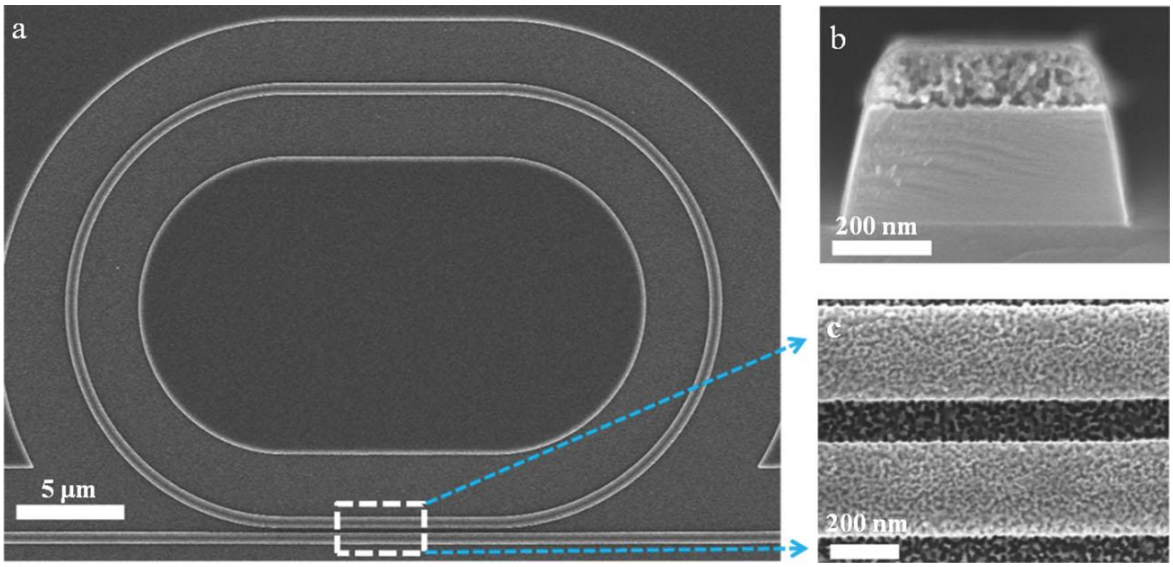


**Figure 5.** pSi-clad SOI racetrack resonator generated using the magnesiothermic reduction of a $SiO_2$ layer on dense Si. a) Top-down secondary electron image of the racetrack resonator. b) Secondary electron image of a cross-section of the pSi-clad SOI waveguide. c) Top-down secondary electron image of the coupling region of the racetrack resonator and the waveguide.

wide by ~230 nm tall silicon waveguide (**Figure 5b**). This geometry was chosen to ensure single-mode operation under transverse electric (TE) polarization (electric field in the device plane) at 1550 nm, while maintaining a reasonably high Q-factor and wide free spectral range. The thin pSi cladding enables a higher loading of analyte molecules within the evanescent tail of the optical mode. Indeed, the large internal specific surface area (≥500 $m^2/g$) associated with uniformly-distributed, nanoscale pores in the pSi film formed by this process provides for greater adsorption of small analytes for enhanced detection sensitivity, while the thin, uniform nature of the pSi films allows for high Q-factors and high spectral resolution.

The TE transmission spectra of such a pSi-clad racetrack resonator and a reference racetrack resonator lacking pSi are shown in **Figure 6a** and **b**, respectively. The full-

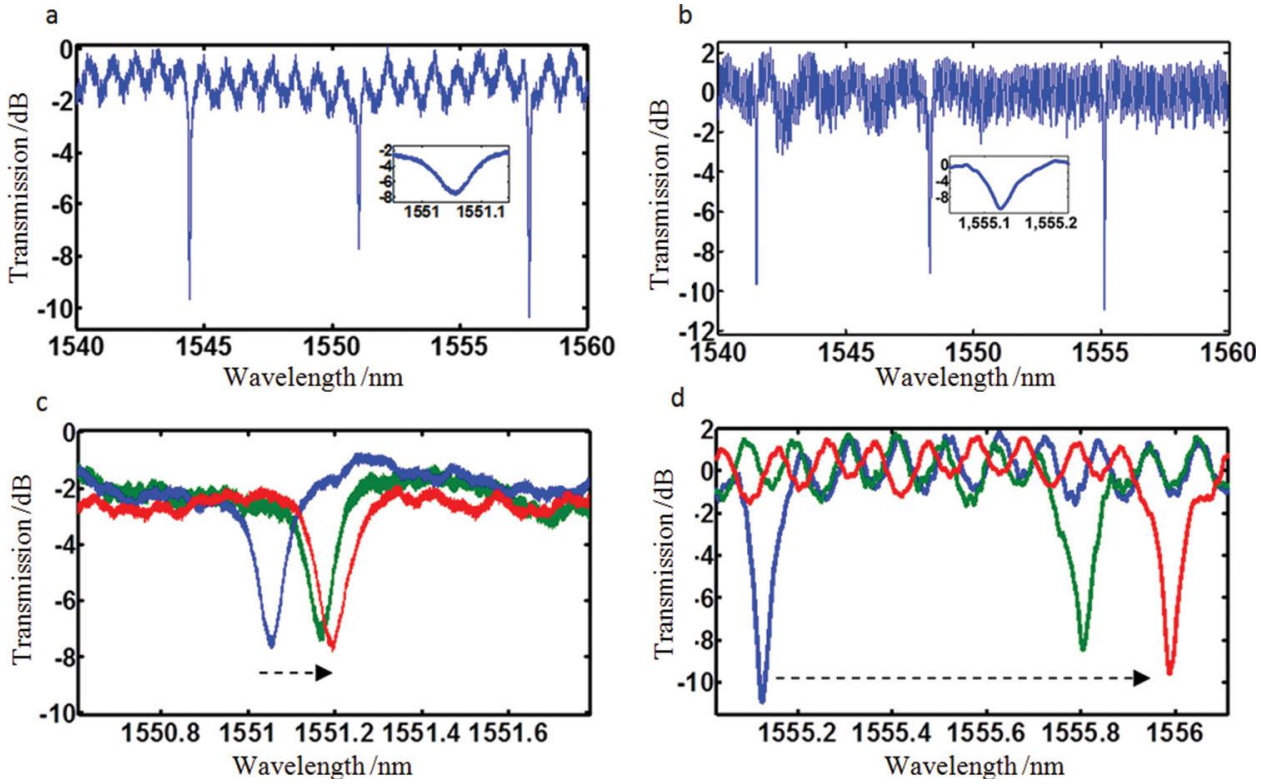


**Figure 6.** Optical characterization of a reference (without pSi) resonator (a),c)) and pSi-clad resonator (b),d)) under TE polarization. a) Transmission spectrum of the reference resonator. (Inset) close-up of the resonance dip around 1550 nm, with a measured FWHM of ~65 pm. b) Transmission spectrum of the pSi cladded resonator. (Inset) close-up of the resonance dip around 1550 nm, with a measured FWHM of ~70 pm. c) Transmission spectra of the reference resonator when no coating was applied (blue), with an APTES coating (green), and with NHS-biotin applied (red). d) Transmission spectra of the pSi-clad resonator when no coating was applied (blue), with an APTES coating (green), and with NHS-biotin applied (red).

width-at-half-maximum (FWHM) of the resonance at 1550 nm for the pSi-clad and reference resonators were ~70 pm and ~65 pm, respectively, which corresponded to loaded Q-factors of 22,000 and 24,000, respectively. To quantitatively evaluate the enhanced analyte adsorption resulting from the increased surface area of the pSi cladding, (3-aminopropyl)triethoxysilane (APTES) monolayers were deposited on pSi-

bearing and reference resonators. Ellipsometric analysis indicated that the deposited APTES thickness was ~9.2 ± 1 Å. After APTES deposition, the redshift in resonance wavelength (**Figures 6d** and **c**) for the pSi-clad resonator (~679.6 pm) was ~6 times larger than for the reference resonator (~112.9 pm). The APTES-induced redshift for the pSi-bearing resonator corresponded to a sensitivity of ~0.8 pm/(pg/mm$^2$). With the Q-factor of the pSi-clad microresonator being 22,000 and a reasonably assumed spectral resolution of ~1 pm, the detection limit of the present pSi-clad sensor, in terms of deposited molecule thickness, was estimated to be ~0.01 Å, which is an order of magnitude better than previously- reported for anodization-derived pSi optical sensors. As a further test of enhanced sensitivity with the pSi cladding, a layer of *N*-hydroxy-succinimidobiotin (NHS-Biotin) was applied via succinimide-crosslinking to the amine-terminated APTES monolayer on both devices. The thickness of the NHS-Biotin layer was determined to be ~3.5 ± 1 Å by ellipsometry (using a refractive index of 1.46). The measured resonance wavelength redshift for the pSi resonator (~183.9 pm) was again about 6 times greater than for the reference resonator (~28.8 pm) (**Figures 6d** and **c**).

Such integrated pSi-bearing SOI microresonator sensors may be applied for the sensitive, reliable, rapid, low-cost, lab-on-chip detection of a variety of potential analytes. This magnesiothermic reaction process and platform may also be applied to devices involving other light-matter interactions (such as nonlinear optics, switching, etc.) for various applications.

### *C. Conformal Coating and Replication:* Porous Wall, Nanocrystalline $TiO_2$ Nanotube Arrays for Solar Cells and Other Electrode Applications

High-aspect-ratio transition metal oxide nanotube arrays with a high density of well-aligned pore channels and high surface areas can be attractive structures for use in a number of chemical, electrical, electrochemical, optical, photochemical, and biochemical devices, such as high-throughput (photo)catalysts or adsorbants, aligned electrodes for solar cells or batteries, sensitive and rapid gas detectors, precise fluid flow control devices, or functionalized membranes for selective (bio)molecular separation.

The Sandhage group has developed an aqueous, protein-enabled, layer-by-layer (LbL) deposition process for generating aligned nanotube arrays comprised of nanocrystalline oxides with a high degree of interconnected porosity present within the tube walls. With this process, repeated alternating exposure of an aligned-nanochannel template to the protein and then to a water-soluble precursor salt is used to build up a conformal protein/oxide composite coating of a desired thickness. Upon subsequent pyrolysis of the protein, a coating comprised of a co-continuous network of pores and oxide nanoparticles is formed. Selective dissolution of the underlying template through the interconnected pore network of the coating then yields freestanding, high-aspect-ratio, porous-wall nanotube arrays. Unlike gas-phase atomic layer deposition, this protein-based process does not require the use of vapor precursors, controlled atmospheres, or vapor-generating equipment. Furthermore, this biomimetic mineralization process does not utilize moisture-sensitive precursors (e.g., the alkoxides used in sol-gel processing)

and does not require hydroxyl-rich templates or multistep surface functionalization treatments (for enriching templates with hydroxyl groups) needed for the surface sol-gel-based deposition of continuous and conformal coatings.

Prior work by the Sandhage group (in collaboration with the Naik group at the Air Force Research Laboratory, Wright-Patterson Air Force Base) involving the use of bacteriophage display biopanning has indicated that 12-mer peptides enriched in basic residues (arginine, lysine, histidine) were particularly effective at binding to titania *and* at inducing the formation of relatively high yields of Ti-O-bearing precipitates at room temperature from an aqueous titania precursor-bearing (Ti(IV) bisammonium-lactato-dihydroxide, TiBALDH) solution. Protamine, a relatively inexpensive and readily-available arginine-rich protein harvested from a variety of fish (e.g., salmon, herring, trout, and tuna), has also been found by the Sandhage group to be capable of binding to silica and titania, and of inducing the formation of conformal Ti-O-bearing coatings from a TiBALDH-bearing solution. This prior work has led the Sandhage group to develop an aqueous protamine-based LbL coating process for generating high-aspect-ratio, aligned nanotube arrays composed of porous, yet interconnected titania nanoparticles.

A porous anodic alumina membrane was used as the template for such nanotube generation. The aligned pore channels running through this membrane are revealed in the top-down and cross-sectional images in **Figures 7a** and **b**, respectively. Such a

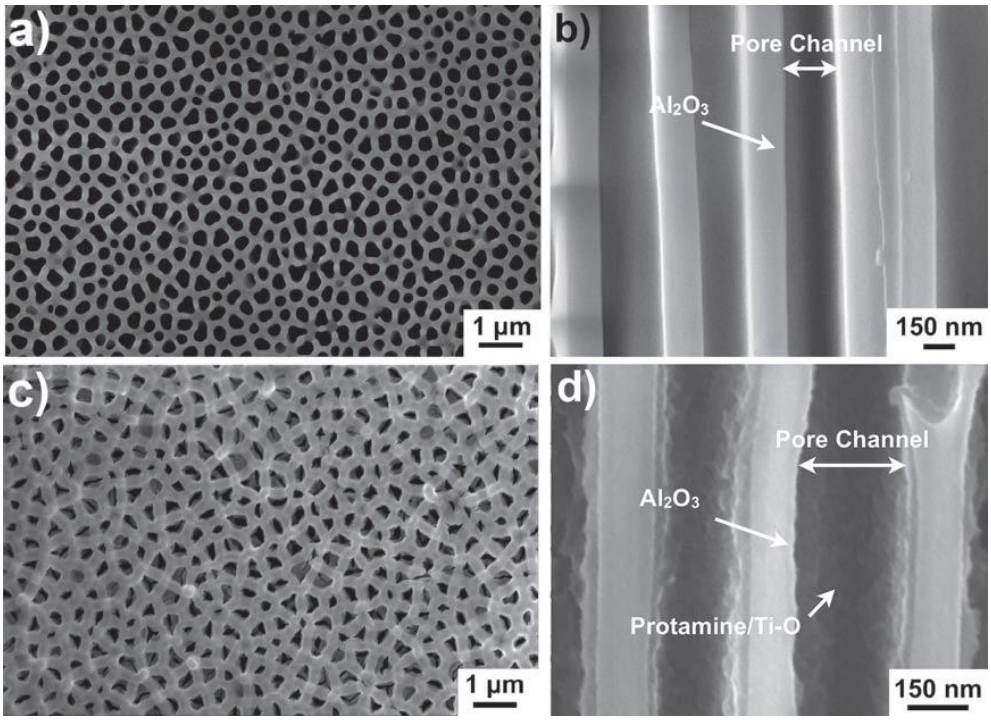


**Figure 7.** Secondary electron images of: a), b) top-down and cross-sectional views, respectively, of an uncoated anodic alumina template and c), d) top-down and cross-sectional views, respectively, of an anodic alumina template covered with a protamine/Ti-O-bearing composite coating after exposure to 8 protamine/TiBALDH deposition cycles.

membrane was exposed to 8 protamine/TiBALDH cycles to buildup a continuous and conformal protamine/$TiO_2$ coating on the external and internal alumina surfaces. Secondary electron images of the coated template are shown in **Figures 7c** and **d**. The cross-section in **Figure 7d** reveals a continuous coating on the alumina template. X-ray photoelectron spectroscopic analyses of such coated surfaces revealed peaks for Ti and O (consistent with titania), N and C (consistent with protamine), but not for Al, which indicated that the protamine/Ti-O-bearing composite coating completely covered the template surface. The protamine/Ti-O-coated alumina membranes were then heated to 650°C in air for 3 h to allow for water removal, organic pyrolysis, and titania crystallization. Thermogravimetric analysis revealed a relatively large weight loss (~44%) from about 200°C to 475°C, which indicated that appreciable protamine was entrained along with titania in the deposited coating. The appreciable interconnected porosity generated throughout the titania coating upon protamine pyrolysis at 650°C allowed for subsequent penetration of a sodium hydroxide solution for selective dissolution of the underlying alumina template. The structural interconnectivity of the titania nanoparticle network in the fired coating resulted in freestanding, high-aspect-ratio titania nanotube arrays (9.9 μm length:34 nm wall thickness = 291:1) upon removal of the alumina template. The titania nanotube arrays were then transferred to transparent, fluorine-doped tin oxide (FTO) coated glass substrates. Prior to attachment of a given nanotube array to such a substrate, the FTO layer was coated with a thin layer of titania nanoparticle-bearing paste. After mating the nanotube array to the coated FTO/glass substrate, the assembly was heated in air to 500°C for 1 h to pyrolyze the organic material in the paste and to sinter-bond the titania nanotube array to the titania nanoparticle-coated FTO/glass substrate. Side-view secondary electron images of a titania nanotube array attached to a FTO/glass substrate are shown in **Figures 8**. The higher magnification image in **Figure 8b** indicates that the freestanding titania tubes were comprised of a porous, yet interconnected network of nanoparticles with diameters of ~15–20 nm. X-ray diffraction analysis of the tubes (**Figure 9a**) yielded

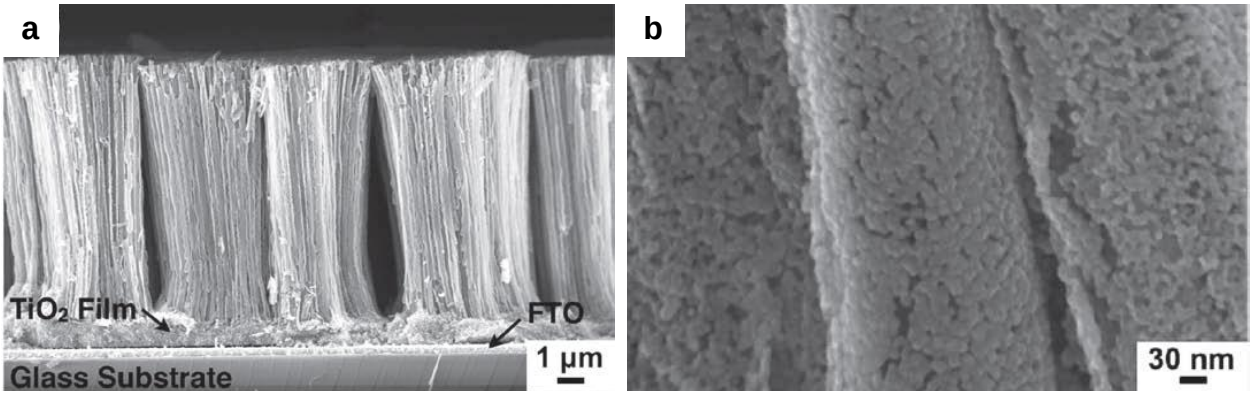


**Figure 8.** Secondary electron images of cross-sectional views of freestanding $TiO_2$ nanotube arrays synthesized via exposure of an anodic alumina template to 8 protamine/TiBALDH cycles, firing at 650°C for 3 h in air, selective dissolution of the alumina template in a NaOH solution (through the pores in the coating), transfer of the $TiO_2$ nanotube array to a $TiO_2$-coated FTO-bearing glass substrate, and then firing at 500°C for 1 h in air.

peaks for anatase titania. Scherrer analysis of the anatase diffraction peaks yielded an average crystallite size of 15 nm, which indicated that the titania crystals and titania particles seen in **Figure 8b** were of comparable size. Transmission electron microscope images (**Figures 9b** and **c**) indicated that the freestanding titania nanotubes were composed of a porous network of nanoparticles with sizes on the order of 10–20 nm (consistent with Scherrer analysis). High resolution transmission electron microscopy (**Figure 9d**) and selected area electron diffraction analysis (**Figure 9e**) yielded lattice fringes and ring patterns, respectively, consistent with nanocrystalline anatase titania.

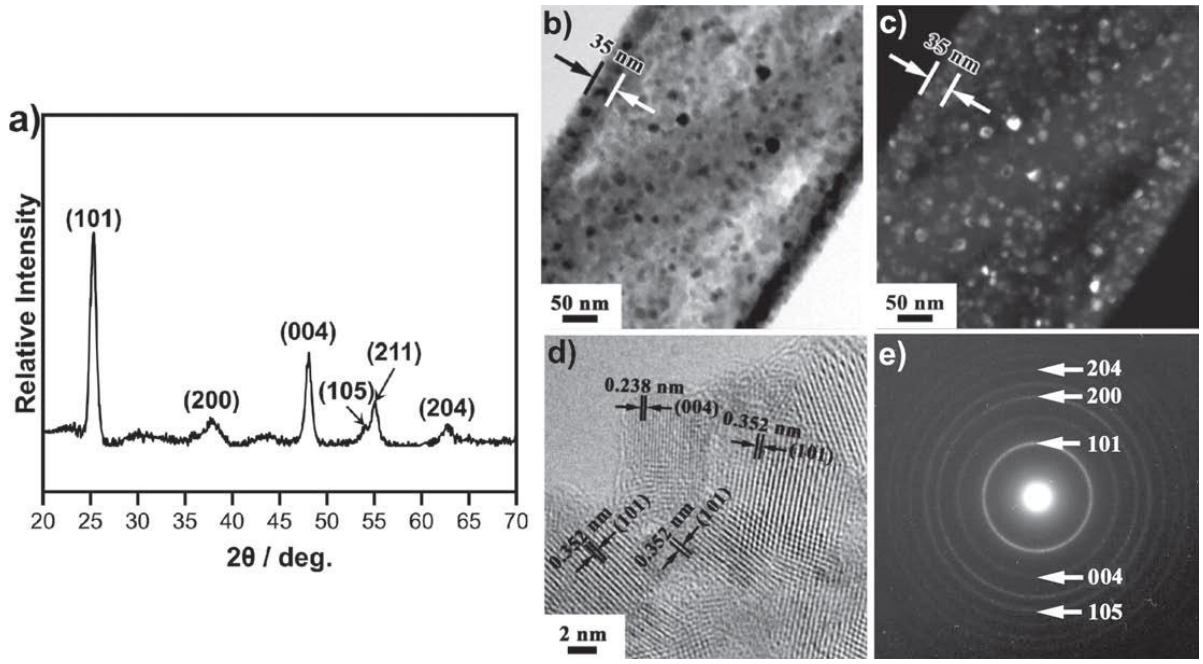


**Figure 9.** a) X-ray diffraction pattern obtained from a titania nanotube array synthesized via exposure to 8 protamine/TiBALDH cycles and then firing at 650°C for 3 h in air (hkl values correspond to diffraction peaks associated with anatase titania). b) Bright field and c) dark field transmission electron images of the cross-section of a titania nanotube in such an array. d) High resolution transmission electron image and e) selected area electron diffraction analysis of the titania nanotube shown in b) and c).

Experiments were then conducted to evaluate the extent of adsorption of a ruthenium-based dye onto the porous nanotube arrays. A N719 dye (cis di(thiocyanato)-N-N'-bis(2,2'-bipyridyl-4-carboxylic acid-4'-tetrabutylammonium carboxylate) ruthenium (II)) was allowed to adsorb onto the porous titania nanotubes for a period of 24 h. The dye was then desorbed from the nanotubes by immersing the assembly in a 100 mM NaOH solution. The concentration of the dye in this solution was evaluated via measurement of the absorbance of the solution at 513 nm and comparison to calibration solutions of known N719 content. The average N719 dye loading was found to be $1.63 \times 10^{-4}$ mol/g (normalized to the weight of titania in the nanotube assembly), which was more than twice the amount of such N719 ruthenium dye adsorbed onto dense wall titania nanotube arrays ($7.42 \times 10^{-5}$ mol/g) prepared via a sol-gel infiltration process.

This work demonstrates that protamine's ability to bind to alumina and titania, as well as its ability to induce the room temperature precipitation of a Ti-O-bearing coating from an aqueous precursor solution, enables the layer-by-layer syntheses of aligned high-aspect-ratio titania nanotube arrays composed of co-continuous networks of pores and titania nanoparticles. These nanotube arrays exhibit: i) enhanced loading of functional molecules (resulting from the interconnected pores in the freestanding nanotube walls), ii) highly-aligned pore channels (resulting from the lateral connectivity of the conformal titania coating deposited at the top and bottom faces of the aligned pore template), and iii) anisotropic electrical conductivity (enabled by the interconnected titania nanoparticle These inherent characteristics of protein-enabled nanotube arrays make them attractive for use as electrodes (solar cells, batteries), sensors, adsorbants, (photo)catalysts, and other electrochemical, photochemical, or biochemical devices.

## II. Bio-enabled, Chemically-Tailored, Hierarchically-Structured Materials

A second major research thrust of the Sandhage group is the bio-enabled syntheses of materials (via the use of biogenic templates and/or biomolecules) with unprecedented combinations of complex chemistry and complex hierarchical (nano-to-macroscale) structure. Nature provides impressive examples of organisms capable of forming organic and inorganic structures with intricate and controlled three-dimensional (3-D) hierarchical (nanoscale-to-macroscale) morphologies. For example, certain butterflies and beetles generate chitinous scales with intricate 3-D structures for exquisite control of color (so-called "structural color"). Among the most versatile of organisms for generating complex inorganic structures are diatoms, a type of aquatic single-celled algae. Each diatom species forms a $SiO_2$-bearing microshell (frustule) with a particular 3-D shape and with specific patterns of fine features (pores, ridges, channels, protuberances, etc.). Owing to the species-specific nature of diatom $SiO_2$ structure formation, a rich variety of 3-D microshell morphologies can be found among the estimated $10^4$-$10^5$ extant diatom species. The sustained reproduction (repeated doubling) of a given species of diatom can yield enormous numbers of daughter diatoms with similarly-shaped frustules (e.g., 80 reproduction cycles corresponds to $2^{80} \approx 1.2 \times 10^{24}$ = twice Avogadro's number of frustule copies). Such massively-parallel, direct, and precise (genetically-controlled) self-assembly of structures with a wide selection of 3-D nano-to-microscale morphologies under ambient conditions has no analogue among synthetic self-assembly processes. However, the $SiO_2$-based chemistry of diatom microshells, and the chitin-based chemistry of butterfly and beetle scales, severely limit the properties and range of applications for such biogenic structures.

The Sandhage group has pioneered and patented several approaches for altering the chemistries, while retaining the 3-D hierarchical morphologies, of these biologically-derived structures. By coupling the impressive structure-formation capabilities (massively-parallel, genetically-precise, 3-D self-assembly) of biological organisms with the wide range of non-naturally-occurring synthetic chemistries (via the Biological Assembly and Shape-preserving Inorganic Conversion or BASIC paradigm), a rich

variety of functional, bio-enabled hierarchically-structured materials may be generated, as illustrated in the following examples.

### *A. Diatom-Enabled 3-D Materials:* Si, C, $TiO_2$, and Other Replicas via Gas/Solid Reactions for Battery and Fuel Cell Electrodes, Enzyme Supports, and Sensors

While diatoms generate a wide variety of selectable, species-specific hierarchical structures that can be attractive for particular uses in energy, environmental, and sensing applications, the $SiO_2$-based chemistry of such structures does not provide the desired electrical, catalytic, and adsorptive properties desired for such applications. To overcome this limitation, the Sandhage group has developed and utilized a variety of shape-preserving reactions (gas/solid, liquid/solid, solid/solid reactions) to convert diatom silica (and synthetic silica) structures into replicas comprised of other functional materials, including Si, C, SiC, MgO, $TiO_2$, $ZrO_2$, $BaTiO_3$, Eu-doped $BaTiO_3$, and Mn-doped $Zn_2SiO_4$. For example, the following magnesiothermic reaction has been used to completely convert such $SiO_2$ structures into MgO/Si replicas:

$$SiO_2(s) + 2Mg(g) => 2MgO(s) + Si(s)$$

Selective acid dissolution of the MgO product then yielded a highly-porous, nanocrystalline Si replica (**Figure 10a**) of the starting diatom $SiO_2$ microshell. The specific surface area of the Si replica was 540 $m^2/g$ (i.e., more than 300 times greater than for the starting $SiO_2$ microshell). The porous Si replica was then converted into a porous C replica (**Figure 10b**) of even higher surface area (1370 $m^2/g$) via the following series of reactions:

$$Si(s) + CH_4(g) => SiC(s) + 2H_2(g)$$

$$SiC(s) + 2Cl_2(g) => C(s) + SiCl_4(g)$$

$TiO_2$ frustule replicas (**Figure 10c**) have been synthesized via the following sequential gas/solid reactions:

$$SiO_2(s) + 2TiF_4(g) => 2TiOF_2(s) + SiF_4(g)$$

$$TiOF_2(s) + H_2O(g) => TiO_2(s) + 2HF(g)$$

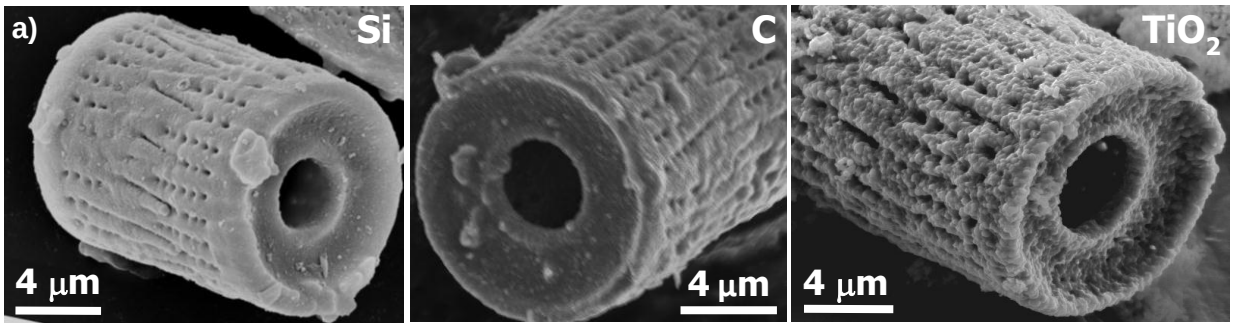


**Figure 10.** Secondary electron images of: a) porous Si, b) porous C, and c) $TiO_2$ replicas of *Aulacoseira* diatom frustules generated via shape-preserving gas/solid reactions.

The use of such shape-preserving reactions to generate Si, SiC, C, $TiO_2$, and other replicas of such biogenic (as well as synthetic) structures has been pioneered and patented by the Sandhage group.

The ability to generate such open, porous, 3-D hierarchical structures comprised of nanocrystalline Si, C, $TiO_2$, and other functional materials with a wide variety of selectable, well-controlled morphologies is quite unique and highly attractive for electrodes (e.g., for lithium ion batteries or fuel cells), catalysts/catalyst supports, sensors, filtration media, and other devices. For example, Pt was deposited onto/into the C frustule replicas with the use of $Pt(CO)_2Cl_2$ vapor, and the electrocatalytic behavior of the resulting nanocrystalline Pt/C frustule replicas (**Figure 11a, b**) for the

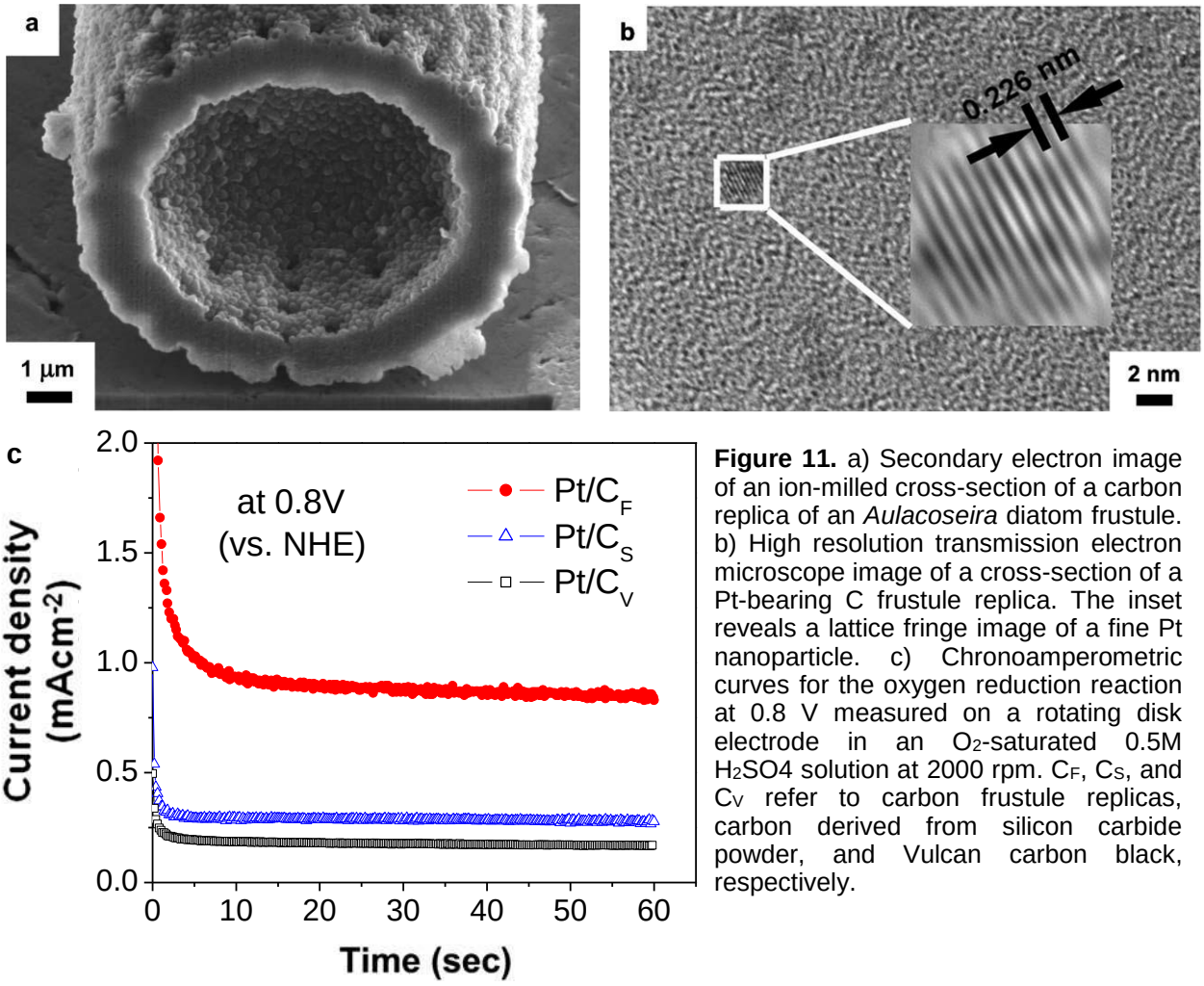


**Figure 11.** a) Secondary electron image of an ion-milled cross-section of a carbon replica of an *Aulacoseira* diatom frustule. b) High resolution transmission electron microscope image of a cross-section of a Pt-bearing C frustule replica. The inset reveals a lattice fringe image of a fine Pt nanoparticle. c) Chronoamperometric curves for the oxygen reduction reaction at 0.8 V measured on a rotating disk electrode in an $O_2$-saturated 0.5M $H_2SO4$ solution at 2000 rpm. $C_F$, $C_S$, and $C_V$ refer to carbon frustule replicas, carbon derived from silicon carbide powder, and Vulcan carbon black, respectively.

oxygen reduction reaction was evaluated in an oxygen-saturated 0.5 M $H_2SO_4$ solution using a rotating disk electrode (via collaboration with Liu, School of Materials Science & Engineering, Georgia Tech). The performance of the Pt-bearing C frustule replicas ($C_F$) was compared with that of Pt-bearing C derived from SiC powder ($C_S$) and Pt-bearing Vulcan XC-72R carbon ($C_V$) black (note: the microparticle content deposited onto the working electrode was adjusted to achieve a similar amount of total platinum loading for

each type of carbon microparticle). As can be seen in **Figure 11c**, the steady-state current for the Pt-bearing C frustule electrode was significantly higher than for the Pt/$C_S$ and Pt/$C_V$ electrodes. Such enhanced electrocatalytic activity of the Pt-bearing C frustule replicas for the oxygen reduction reaction was consistent with the presence of a higher population of very fine (<2 nm diameter) Pt nanoparticles (**Figure 11b**) and a reduced oxygen diffusion distance (due to the hollow nature and thin wall inherited from the starting diatom frustule, **Figure 11a**) for these microparticles than for the Pt/$C_S$ and Pt/$C_V$ microparticles. That is, synergistic use of the bio-enabled hierarchical frustule structure with the new synthetic Pt/C chemistry and nanostructure yielded enhanced electrocatalytic performance.

Such control over 3-D morphology and chemistry/nanostructure allows for the tailoring of fluid (gas or liquid) transport through, and nanoparticle dispersions within, highly porous carbon structures for enhanced catalysis, filtration, intercalation, or adsorption for numerous applications, such as in energy storage and harvesting, sensing, water purification, carbon sequestration, and (bio)chemical separation.

### *B. Diatom-Enabled 3-D Materials:* Au Replicas via Conformal Electroless Deposition for Extraordinary Optical Transmission

Nanocrystalline plasmonic materials, such as gold or silver, can exhibit remarkable optical and chemical properties if fabricated in an appropriate structure. For example, gold or silver films possessing patterned arrays of pore channels can exhibit appreciable light transmission even if the pore channel diameters are appreciably smaller than the wavelength of the transmitted light. Such surface plasmon-enabled “extraordinary optical transmission” is strongly affected by the pore channel pattern and spacing. To evaluate the utility of patterned pore structures generated by diatoms for such light transmission, the Sandhage group (in collaboration with the Perry group, School of Chemistry & Biochemistry at Georgia Tech) has examined the conversion of diatom $SiO_2$ frustules into replicas comprised of nanocrystalline Au and other metals. The frustules of the *Coscinodiscus asteromphalus* diatom (cultured in the Sandhage laboratory) were selected, owing to the quasi-periodic pore pattern present on such frustules (**Figure 12**). To allow for electroless gold deposition, the surfaces of the silica

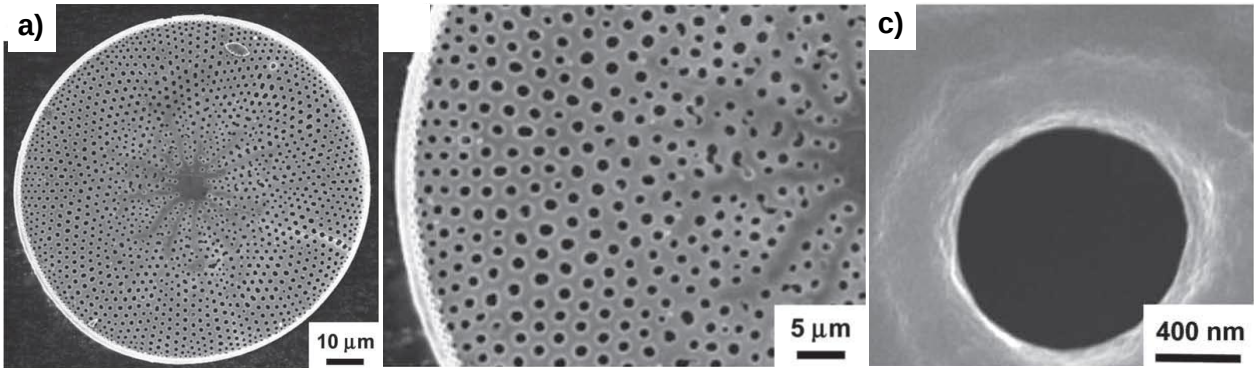


**Figure 12.** Secondary electron images of the silica frustule of the centric diatom *Coscinodiscus asteromphalus*. The valve of this frustule contains a quasi-periodic (hexagonal) array of pore channels.

frustules were first functionalized with a high density of catalyst particles. A thin, conformal, and continuous layer of nanocrystalline gold was then deposited onto the frustules during immersion in an electroless gold plating solution. The underlying silica template was then removed by selective dissolution through occasional pinholes in the metal coating. Secondary electron images of the resulting high-fidelity gold replica of the *C. asteromphalus* frustule are shown in **Figure 13**. An

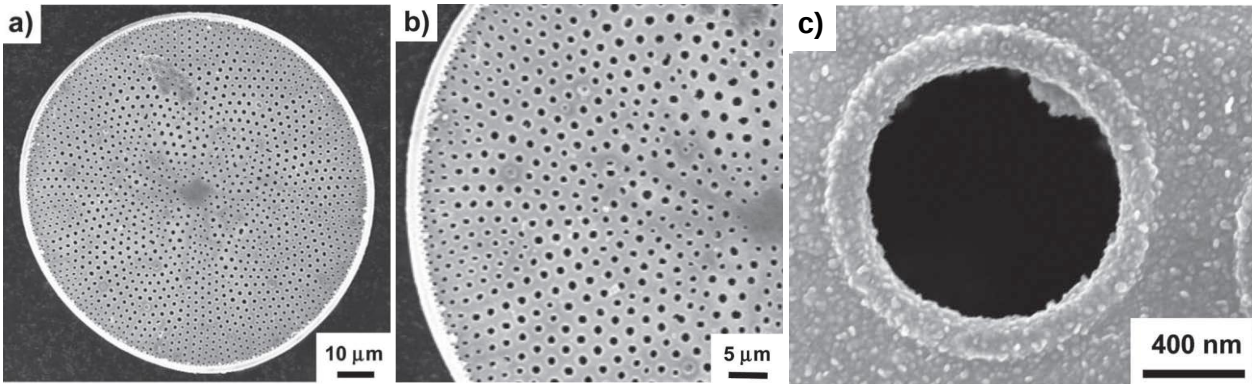


**Figure 13.** Secondary electron images of a freestanding (silica-free) gold replica of the silica frustule of the centric diatom *Coscinodiscus asteromphalus*.

optical image of the gold frustule replica, and the transmission of infrared light through the replica, are shown in **Figure 14**. A range of IR wavelengths, centered about 4.3 μm (peak transmission of 13%) could be transmitted through this frustule, even though the average pore channel diameter was well below 4 μm (on the order of 1 μm). Such multiwavelength extraordinary IR transmission resulted from the synergistic use of a bio-enabled structure and the shape-preserving conversion of such a structure into a nanocrystalline gold replica. Bio-enabled structures of this type can be attractive for optical filtering, sensing, catalysis, and other applications.

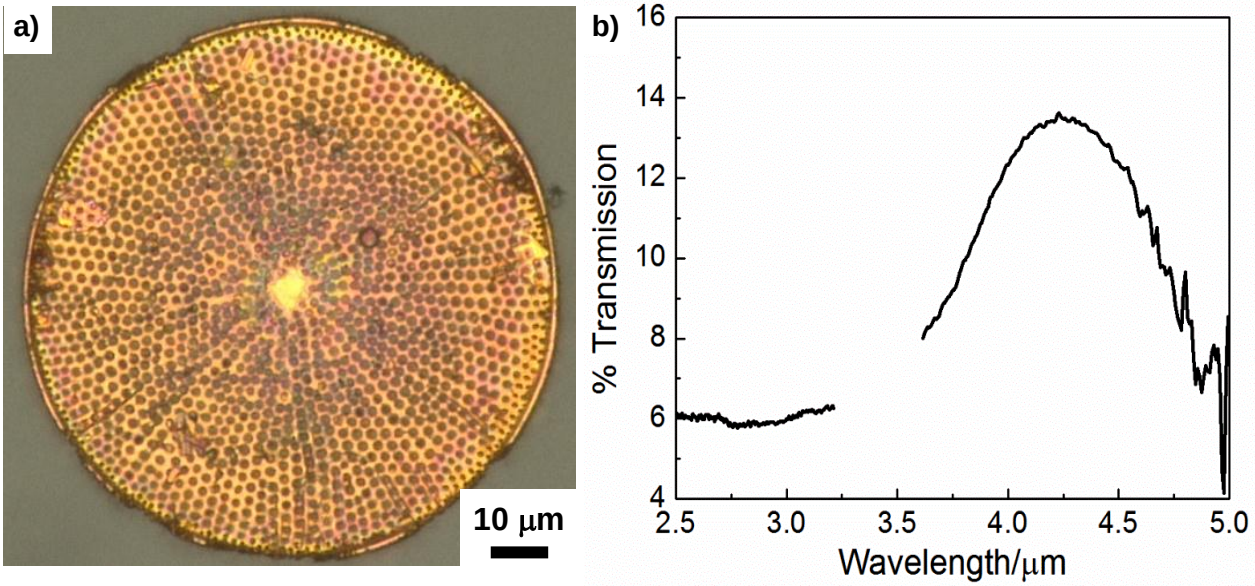


**Figure 14.** a) Optical image of a freestanding ($SiO_2$-free) Au replica of the frustule of the centric diatom *Coscinodiscus asteromphalus*. b) Transmission spectrum obtained from the gold frustule replica in a).

### *C. Butterfly-Enabled 3-D Materials:* Photoluminescent Eu-doped $BaTiO_3$ Replicas via Layer-by-Layer Surface-Sol-Gel Coating and Hydrothermal Reaction for Anti-Counterfeiting and Tracking

Certain butterflies, moths, and beetles exhibit impressive control of color through the use of hierarchically-patterned 3-D chitinous structures. To expand the range of optical properties exhibited by such structures, the Sandhage group has developed strategies for converting such assemblies into functional inorganic replicas that retain the intricate biogenic morphologies. For example, such chemical conversion has been applied to the scales within the blue-green stripes on the dorsal forewings and hindwings of the *Papilio blumei* butterfly (**Figure 15**). Bright field optical images of these stripes (**Figure 15a** inset) reveal overlapping tapered scales with typical lengths of about 200 μm and

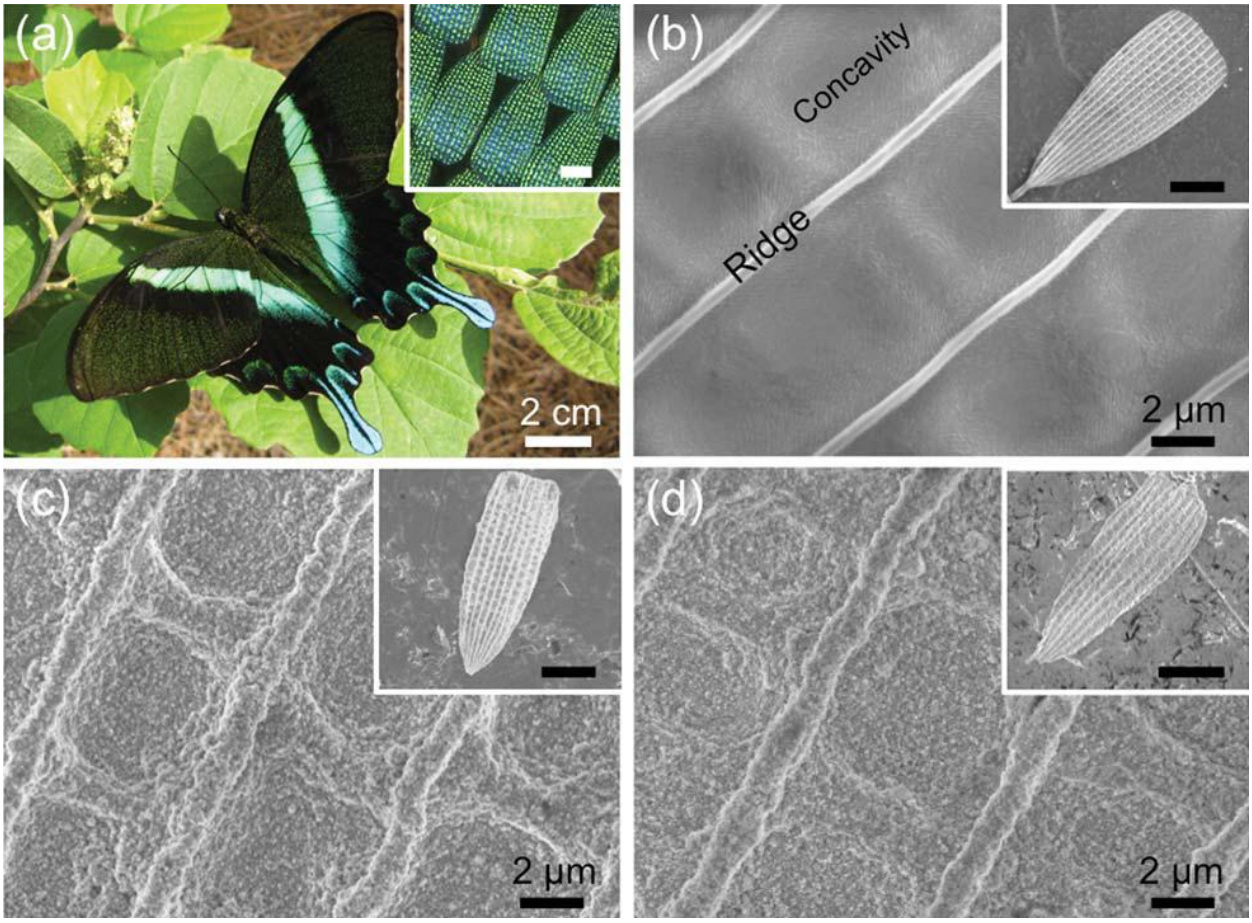


**Figure 15.** a) Optical image of a *Papilio blumei* butterfly, with an inset showing a bright field optical image of the blue-green scales. Secondary electron images of: b) a native blue-green scale, c) a $BaTiO_3$ scale replica, and (d) a Eu-doped $BaTiO_3$ scale replica, with inset images of entire scales. All inset scale bars = 50 μm.

maximum widths of about 100 μm. Each individual scale (**Figure 15b**) contained elevated ridges running parallel to the scale length, with shallow concave depressions lying between the ridges. The hydroxyl-rich nature of the chitin that comprises such

scales enabled the highly-conformal, layer-by-layer coating of such scales with titania via the surface sol-gel process, using a computer-automated deposition system developed by the Sandhage group. After 50 deposition cycles, the coated scales were heated in air to 450$^{o}$C for 4 h to allow for pyrolysis of the chitin template and crystallization of the $TiO_2$. The resulting $TiO_2$ replicas were then converted into Eu-doped $BaTiO_3$ replicas via microwave hydrothermal reaction with a solution of europium and barium acetates at 140$^{o}$C. As shown in **Figures 15c** and **d**, the converted (all-inorganic) scales retained the raised ridges and shallow concave depressions of the native *P. blumei* scales along with the overall tapered scale shape.

Confocal fluorescence microscopy was used to evaluate the patterned photoluminescence of the Eu-doped $BaTiO_3$ *P. blumei* scale replicas. A fluorescence image (488 nm excitation with a long-pass 585 nm filter), a transmission optical image (543 nm light), and a composite (fluorescence + transmission) image of a Eu-doped $BaTiO_3$ scale replica are shown in **Figure 16**. The fluorescence image of the Eu-doped $BaTiO_3$-converted scale clearly revealed the tapered scale shape and parallel microscale ridge pattern of the *P. blumei* scales. The similarities between the

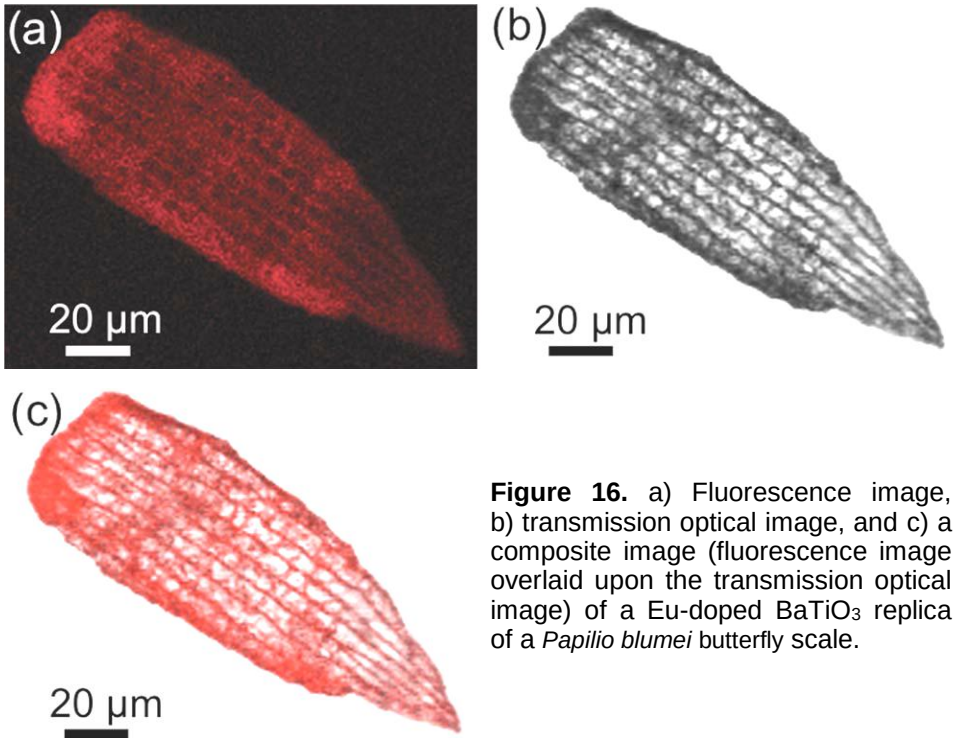


**Figure 16.** a) Fluorescence image, b) transmission optical image, and c) a composite image (fluorescence image overlaid upon the transmission optical image) of a Eu-doped $BaTiO_3$ replica of a *Papilio blumei* butterfly scale.

fluorescence and transmission optical images were consistent with a relatively uniform distribution of Eu throughout the replica. The utility of such 3-D Eu-doped $BaTiO_3$ structures for unobtrusive labelling of white paper was then examined. A bright field optical image, and an associated fluorescence image, of the same scales on white filter paper are shown in **Figure 17**. The inset images shown in these figures were obtained with the scales placed on a glass slide. A 3-D topographical color map of Eu-doped $BaTiO_3$ scale replicas on the filter paper, generated from a series of stacked confocal

dark field images, is also shown in **Figure 17c**. The topographical map revealed that the inorganic scale replicas were able to bend so as to conform well to the surface of the filter paper. Such conformality, along with white color of both the scales and the filter paper, made detection of the scale replicas on the filter paper difficult in visible light, as seen in the bright field image of **Figure 17a**. However, the presence of such scales was readily detected in the fluorescence image of **Figure 17b**.

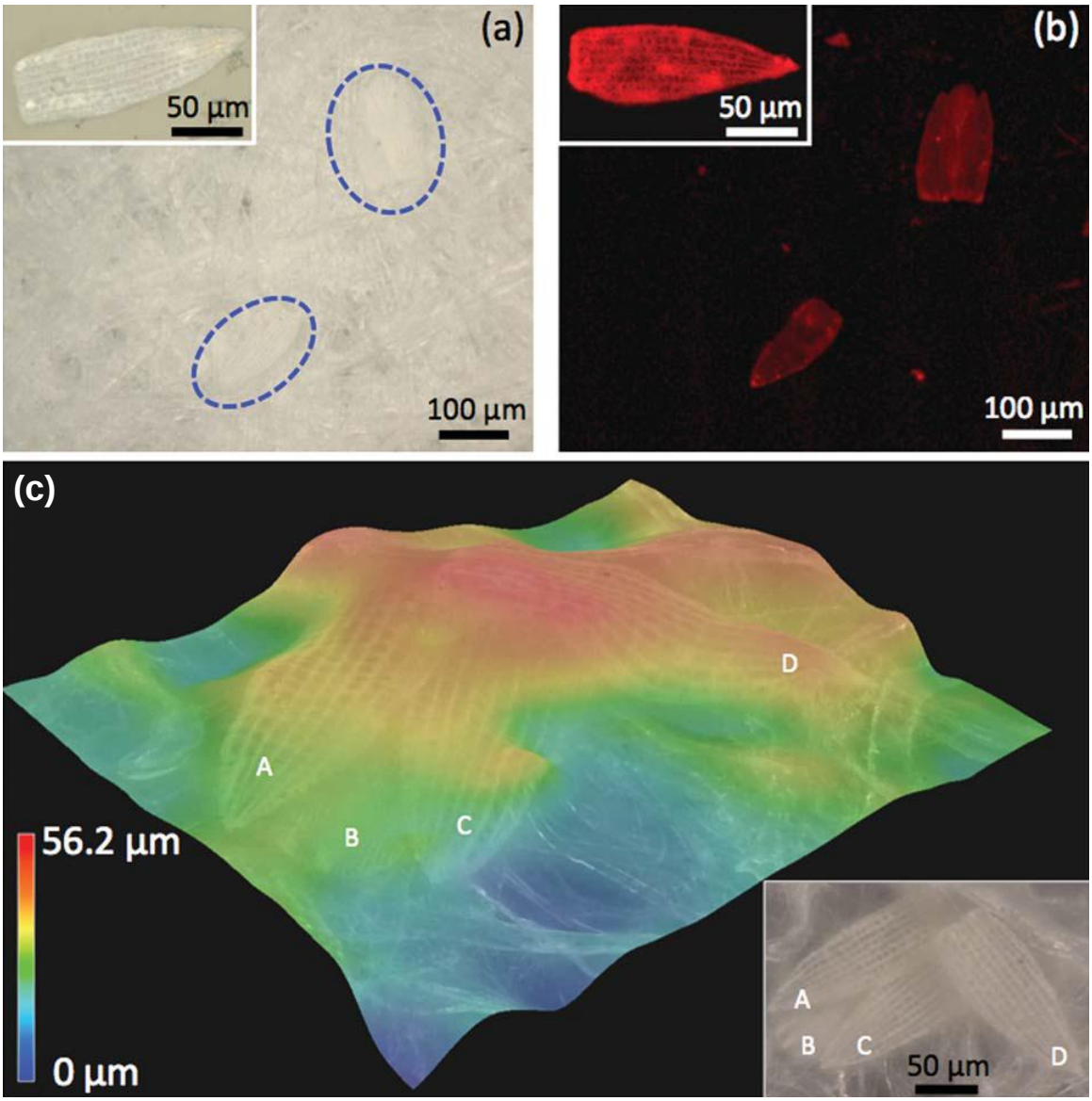


**Figure 17.** a) Bright field and b) fluorescence images of the same Eu-doped $BaTiO_3$ scale replicas on white filter paper, with inset images of Eu-doped $BaTiO_3$ replicas placed on glass slides. c) A topographical color map of Eu-doped $BaTiO_3$ scales A–D deposited onto white filter paper, with a dark field top-down inset image of the same scales.

This 3-D morphology-preserving chemical conversion process provides a means of generating patterned photoluminescent inorganic structures with an enormous variety of morphologies derived from (bio)organic templates and tailorable color(s) (via doping of

$BaTiO_3$ with one or more lanthanides) for unobtrusive, yet highly-distinct labelling of documents or goods for tracking or anticounterfeiting purposes.

### *C. Pollen-Enabled 3-D Materials:* Magnetic $Fe_3O_4$ Replicas via Layer-by-Layer Surface Sol-Gel Coating for Tailored Multimodal Adhesion

Adhesion by or on microparticles plays a critical role in a wide range of developing and mature technologies, including drug delivery, catalysis, water/chemical purification, sensing, antifouling coatings and membranes, semiconductor device processing, composite processing, paints, printing, and xerography. Microparticles with rough surfaces and nonspherical shapes are desired for a number of such technologies. However, the scalable fabrication of microparticles with well-controlled surface asperities in a variety of three-dimensional (3D) morphologies and with tailorable chemistries to allow for tunable adhesion remains a difficult synthetic challenge. A rich sustainable source of 3-D microparticles, with complex morphologies affecting dispersion and adhesion in nature, is pollen. Pollen particles come in a wide variety of 3-D shapes and species-specific surface topographies and are produced in large and increasing quantities worldwide by plants. Because the exine (outer layer) of pollen grains is composed of sporopollenin (a complex polymer consisting of carboxylic acids and aromatic moieties cross-linked with aliphatic chains), the pollen surfaces are enriched with hydroxyl groups that provide an abundance of reaction sites for the chemisorption of alkoxide precursors during a surface sol-gel-coating process.

A computer-automated, layer-by-layer, surface sol-gel process has been developed by the Sandhage group to convert the sporopollenin-based exine of pollen grains into magnetic $Fe_3O_4$ replicas. Secondary electron images of a starting cleaned sunflower pollen grain are shown in **Figure 18a**. The sunflower pollen grains were roughly spherical in shape and possessed echini (spines) of relatively high aspect ratio (height/width-at-mid-height ratio of ~5:1). A secondary electron image of a sunflower pollen particle after exposure to 30 surface sol-gel Fe-O deposition cycles is shown in **Figure 18b**. The highly conformal nature of the surface sol-gel Fe-O-bearing coating was evident from the preservation of the echini and the fine pores at the base of the echini (as indicated by the arrows in **Figure 18b**). The coated pollen particles were then heated in air at 600°C for 4 h to allow for pyrolysis of the pollen template and crystallization of the oxide coating. Complete pyrolysis of the sporopollenin during this treatment was confirmed by thermogravimetric analysis. Although smaller in diameter than the starting as-coated pollen particles, these hematite particles retained the 3-D shapes and surface features of the starting pollen grains (**Figure 18c**). Indeed, the high-fidelity nature of such replication was revealed by images of the same particle before (**Figure 18b**) and after (**Figure 18c**) the 600°C/4 h treatment. (Note that the arrows in **Figures 18b** and **c** reveal the same spine and fine pore present before and after this thermal treatment.) Conversion of these hematite ($Fe_2O_3$) replicas into magnetite ($Fe_3O_4$) was conducted via use of a thermal treatment with a Rhines pack. An excess powder mixture of iron and magnetite was sealed along with hematite pollen replicas

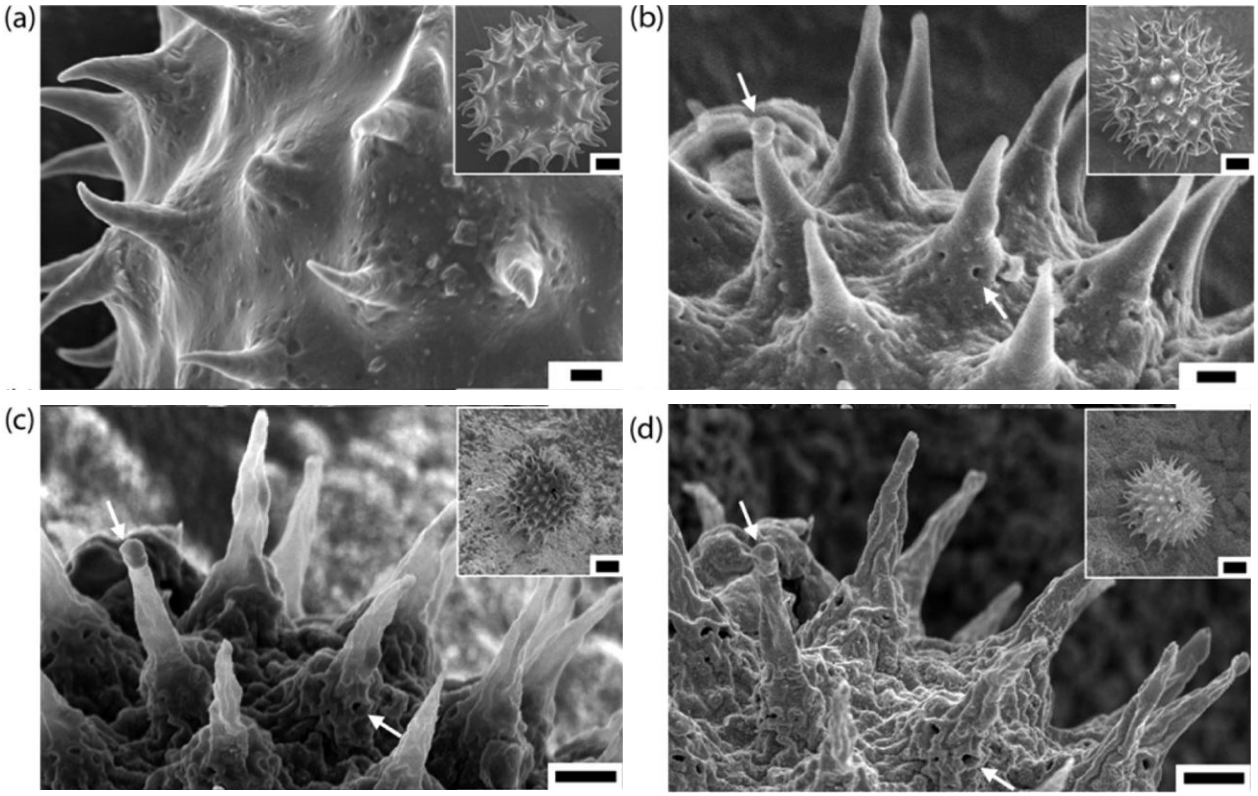


**Figure 18.** Secondary electron images of sunflower pollen particles at various stages of conversion into $Fe_3O_4$: a) the exine of a natural grain, b) an Fe-O-coated grain after 30 SSG deposition cycles, c) an α-$Fe_2O_3$ replica of the same grain in panel b after pyrolysis at 600°C for 4 h in air, and d) a $Fe_3O_4$ replica of the same α-$Fe_2O_3$ grain in panel c generated by partial reduction using a Rhines pack (Fe/$Fe_3O_4$) at 550°C for 3 h. The scale bars indicate 5 μm for the low-magnification insert images and 2 μm for the higher-magnification images.

within a mild steel ampule. The ampule was then heated to 550°C for 2 h. The oxygen partial pressure established within the ampule by the Fe/$Fe_3O_4$ equilibrium at 550°C allowed for complete conversion of the replica particles into phase-pure nanocrystalline magnetite, as confirmed by X-ray diffraction analysis. Scherrer analyses yielded an average magnetite crystallite size of 34 nm. Secondary electron images (**Figure 18d**) indicated that the 3-D morphology and sharp echini of the sunflower pollen were retained by the magnetite replicas. (Note that the arrows in **Figures 18c** and **d** show the same spine and fine pore before and after this Rhines pack thermal treatment.)

To allow for quantitative evaluation of the adhesion of the magnetite pollen replicas to various substrate surfaces, single replica particles were attached to AFM cantilevers (**Figure 19a**). Contact mode AFM measurements were then used (in collaboration with the Meredith group in the School of Chemical & Biomolecular Engineering at Georgia Tech) to evaluate the short-range (van der Waals-based) and long range (magnetic) adhesion of such particles to a variety of substrates, including Si and an axially-poled Nd-Fe-B alloy coated with a thin foil of Ni. As revealed in **Figure 19b**, a similar short-range van der Waals adhesion force of ~40 nN was observed for the $Fe_3O_4$ sunflower pollen particle in contact with either the Si substrate or the Ni-coated Nd-alloy magnet substrate. However, an appreciable additional magnetic attractive force of ~40 nN was

detected between the ferrimagnetic $Fe_3O_4$ sunflower pollen replica and the disk-shaped Ni-coated Nd-alloy substrate at locations near the outer edge of this substrate, which is where the magnetic field intensity associated with this magnetized Ni-Nd substrate was the highest. The magnetic interaction between the $Fe_3O_4$ sunflower pollen replicas and the magnetized edge of the Ni-coated Nd-alloy substrate persisted out to a separation distance of ~1 mm.

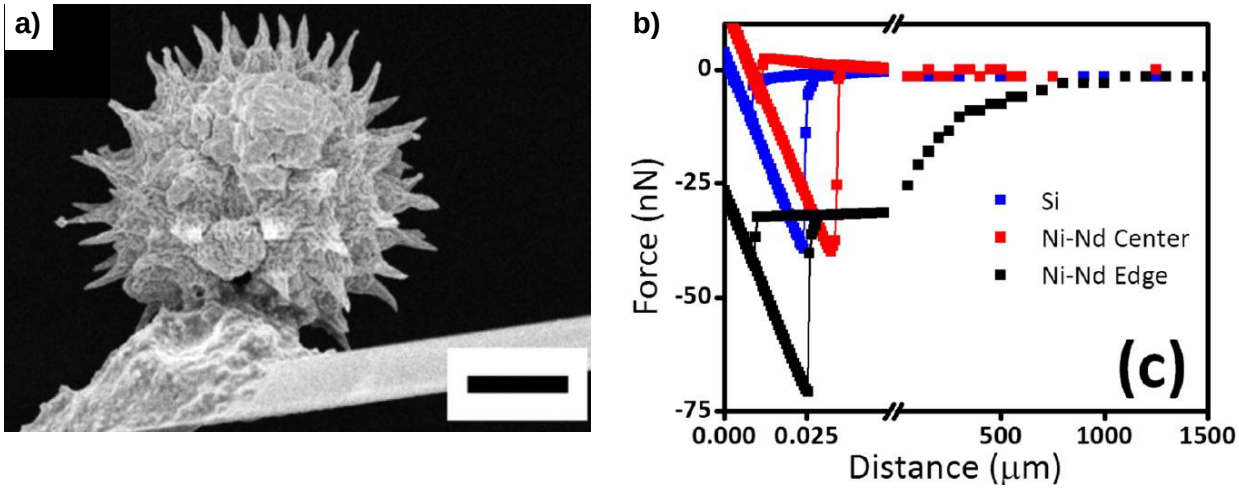


**Figure 19.** a) Secondary electron image of a single $Fe_3O_4$ sunflower replica-bearing cantilever probe used in the AFM adhesion studies. The scale bar indicates 5 μm. b) AFM measurements of the total (VDW + magnetic) adhesion force vs distance for the $Fe_3O_4$ sunflower pollen replica probe with a Si substrate and the Ni-coated Nd-alloy (magnetic) substrate. The Ni-Nd center and Ni-Nd edge refer to analyses obtained at the center and at ~300 μm from the edge, respectively, of the disk-shaped Ni-coated Nd-alloy substrate. The magnetic field intensity at the center of the disk-shaped Ni-coated Nd-alloy was much weaker than at ~300 μm from the edge of this substrate.

This work demonstrates that a highly-conformal, layer-by-layer, surface sol-gel-coating process can be used along with controlled modest-temperature thermal treatments to convert pollen particles into nanocrystalline ferrimagnetic ($Fe_3O_4$) replicas exhibiting multimodal adhesion via short-range van der Waals-based attraction and short-to-long-range (up to ~1 mm) magnetic attraction. The wide variety of 3-D particle shapes and surface topographies available from pollen generated by different plants and the ability of this coating process to produce high-fidelity nanocrystalline replicas with controlled amounts of magnetic oxide (by adjusting the number of deposition cycles) allows for the syntheses of pollen-derived microparticles with highly tailorable multimodal adhesion.

### *D. Protein-Enabled Hybrid Coatings:* Enzyme/Oxide Coatings via Layer-by-Layer Protamine-Based Deposition for Biocatalysis

The protamine-enabled, layer-by-layer deposition process discussed above has also been utilized to generate functional enzyme/oxide coatings. In collaboration with the Kröger group (now at B CUBE Center for Molecular Bioengineering, Dept. Chemistry & Food Chemistry, Technical University of Dresden), a protamine-enabled process has been developed for the controlled immobilization of the model enzyme, glucose oxidase (GOx), on Stöber silica substrates. Protamine (PA) molecules were covalently linked to

GOx using the amine-reactive homobifunctional crosslinking molecule, bis(sulfo-succinimidyl) suberate. At pH 7, the resulting hybrid molecule, GOx-PA, exhibited a positive zeta potential ($\zeta$ = + 5.1 ± 1.0 mV) unlike the GOx molecule alone ($\zeta$ = –2.9 ± 1.6 mV). The layer-by-layer deposition process was then conducted with the use of positively-charged PA or GOx-PA molecules as the binding and mineralizing agents for a given deposition cycle. Coatings with silica (using a freshly-prepared silicic acid precursor from acid hydrolysis of TMOS) or titania (using a TiBALDH precursor) were examined. The influence of the position of the hybrid GOx-PA molecule within 5 layers of deposited coating on the activity of the enzyme (relative to the free GOx-PA molecule in solution) is shown in **Figure 20**. The activities of the different enzyme-bearing samples were dependent on both the particular layer location in which the enzyme was immobilized and the oxide composition of the coating. The activity of the enzyme increased as the enzyme was placed in layers located closer to the outer surface and was modestly higher in Si-O-bearing coatings as compared to Ti-O-bearing coatings. Indeed, GOx-PA immobilized in the fourth of five Si-O-bearing layers (specimen Si4 in **Figure 20**) exhibited essentially the same activity as the enzyme in solution, although a lower activity level resulted when the enzyme was immobilized in Ti-O-bearing coatings (specimen Ti4). The higher apparent enzymatic activity of the Si-O-bearing coatings, for the same layer position within the coating, was attributed to an enhanced rate of glucose diffusion through the Si-O-bearing coatings, due to the higher meso- and macroporosity values and reduced thickness, of Si-O-bearing coatings relative to the Ti-O-bearing coatings.

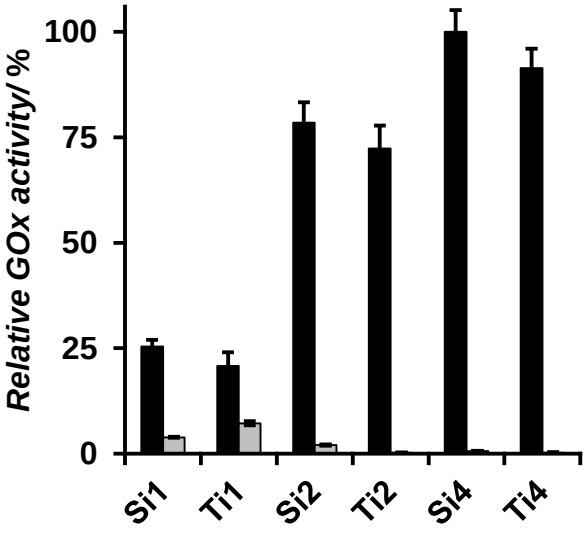


**Figure 20.** Layer position dependence of enzyme activity. Enzyme activities are normalized against the activity of free GOx-PA in solution. GOx-PA has been immobilized *in situ* on Stöber silica particles containing five layers of either Si-O (Si*x*) or Ti-O (Ti*x*) (where *x* refers to the layer in which GOx-PA was immobilized). Enzyme activities bound to the particles (black bars) and in the supernatants (grey bars) were determined. The height of each bar represents the average value from the analyses of three independent samples; the range of values indicated by brackets corresponds to ± one standard deviation about the average value.

To investigate the effect of GOx-PA immobilization within a nanoscale mineral-bearing coating on the thermal stability of the enzyme, Si4 and Ti4 coated particles (i.e., GOx-PA immobilized in the fourth of five layers of Si-O- or Ti-O-coated silica spheres) were incubated at 65°C. Over a period of 48 h, aliquots were periodically removed and assayed for GOx activity. A rapid decrease in enzymatic activity for GOx-PA in solution was observed (**Figure 21a**), with a complete loss of activity after 90 min, which was

consistent with previous results observed for the thermal denaturation of GOx in solution. In contrast, GOx-PA immobilized in Si-O and Ti-O retained 41.4 ± 7.5% and 21.9 ± 1.7% activity, respectively, after 90 min. Even after 3 h of incubation at 65°C, immobilized GOx-PA still exhibited 27.6 ± 4.0% (Si4) and 16.4 ± 2.8% (Ti4) of the original activity (**Figure 21a**). These data demonstrated that GOx-PA molecules immobilized inside Si-O and Ti-O nanoscale coatings were substantially stabilized against thermal denaturation. Inside the oxide films, protein unfolding (with an associated increase in protein volume) may be inhibited, thus stabilizing the native conformation and activity of the enzyme. To test whether this mechanism played a role in thermal stabilization of GOx-PA molecules immobilized within Ti-O-bearing and Si-O-bearing coatings, protease accessibility experiments were performed. GOx-PA-bearing Ti4 and Si4 particles and free GOx-PA were exposed for 24 h to pronase (a highly-active unspecific protease mixture). While >75% of free GOx-PA in solution was degraded, >81% of the immobilized GOx-PA molecules remained active in the Ti4 and Si4 samples (**Figure 21b**). This indicated that GOx-PA molecules were largely inaccessible within the Si-O and Ti-O nanoscale coatings, consistent with the enzyme being contained with nanoscale cavities.

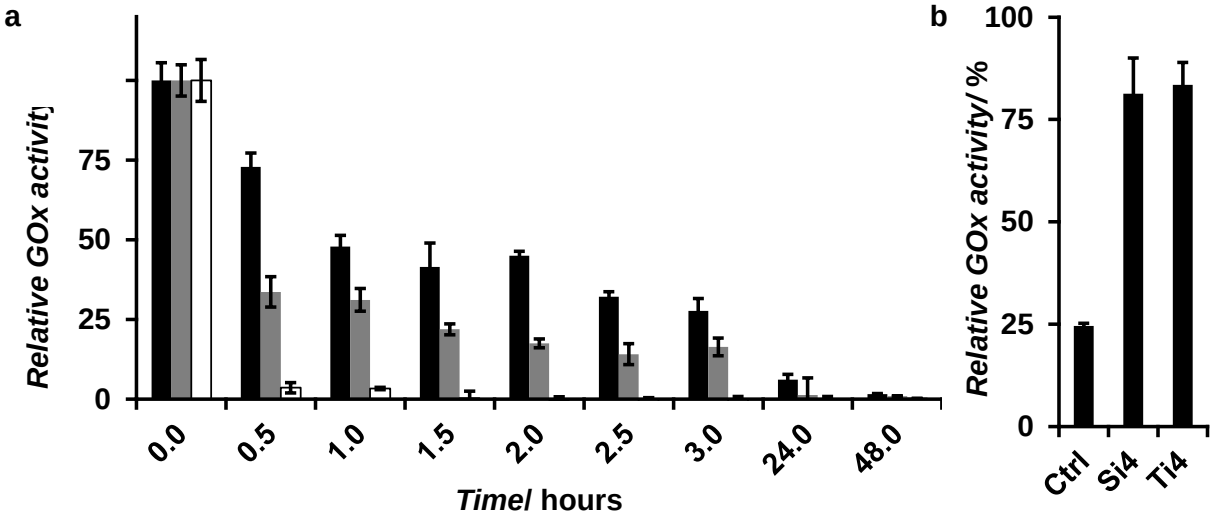


**Figure 21.** Stability of immobilized GOx-PA. GOx-PA was deposited in layer 4 of LbL-mineralized particles containing a total of 5 mineral layers. Activity data were normalized to the sample activity at the beginning of the experiment (0 h). The height of each bar represents the average value from the analyses of three independent samples; the range of values indicated by brackets corresponds to ± one standard deviation about the average value. a) Temperature stability. Time course of thermal deactivation at 65°C of GOx-PA in solution (white bars), immobilized in Si-O (black bars), or Ti-O (gray bars). b) Sensitivity to proteolysis. Enzyme activities of GOx-PA in solution (Ctrl), immobilized in Si-O (Si4), or immobilized in Ti-O (Ti4) after 24 h of incubation with pronase.

This work demonstrates that a protein-enabled layer-by-layer coating process, involving the use of a properly-modified *and* properly-distributed functional enzyme within a nanoscale bio-organic/inorganic composite coating, can allow for full retention of enzymatic activity while providing enhanced stability against thermal and biochemical (protease) degradation. It is envisioned that this general strategy may be utilized to

generate functional and robust biomolecule-bearing nanoscale composite coatings for a variety of highly-demanding (bio)technological applications.